Localized topological changes of the plasma membrane upon exocytosis visualized by polarized TIRFM

Arun Anantharam,[1] Bibiana Onoa,[4,5] Robert H. Edwards,[4,5] Ronald W. Holz,[1] and Daniel Axelrod[2,3]

[1]Department of Pharmacology, [2]Department of Physics, and [3]Department of Biophysics, University of Michigan, Ann Arbor, MI 48109
[4]Department of Neurology and [5]Department of Physiology, School of Medicine, University of California, San Francisco, San Francisco, CA 94143

Total internal reflection fluorescence microscopy (TIRFM) images the plasma membrane–cytosol interface and has allowed insights into the behavior of individual secretory granules before and during exocytosis. Much less is known about the dynamics of the other partner in exocytosis, the plasma membrane. In this study, we report the implementation of a TIRFM-based polarization technique to detect rapid submicrometer changes in plasma membrane topology as a result of exocytosis. A theoretical analysis of the technique is presented together with image simulations of predicted topologies of the post-fusion granule membrane–plasma membrane complex. Experiments on dil-stained bovine adrenal chromaffin cells using polarized TIRFM demonstrate rapid and varied submicrometer changes in plasma membrane topology at sites of exocytosis that occur immediately upon fusion. We provide direct evidence for a persistent curvature in the exocytotic region that is altered by inhibition of dynamin guanosine triphosphatase activity and is temporally distinct from endocytosis measured by VMAT2-pHluorin.

Introduction

The plasma membrane–cytosol interface is a highly specialized domain in which unique and critical cellular functions occur. It is the site of biochemical and ionic signaling through receptors and channels that coordinates cellular processes with the extracellular environment. It is also the site of intercellular interactions, the locus of molecular components important for cell motility, and the site of numerous vesicular trafficking reactions including endocytosis, phagocytosis, viral budding, and exocytosis.

Total internal reflection (TIR) fluorescence (TIRF) microscopy (TIRFM) is superbly suited to visualize the plasma membrane–cytosol interface because the exponentially decaying evanescent field of TIR selectively illuminates the portion of the cell within a distance of 50–100 nm from the glass coverslip upon which the cells reside. TIRFM has been used to characterize the dynamics of fluorescently tagged secretory granules around the time of exocytosis and to visualize individual granule fusion events (Burke et al., 1997; Steyer et al., 1997; Oheim et al., 1998; Han et al., 1999; Tsuboi et al., 2000; Ohara-Imaizumi et al., 2002; Allersma et al., 2004, 2006; Shakiryanova et al., 2005; Silverman et al., 2005; Degtyar et al., 2007). However, the other partner to exocytosis, the plasma membrane, has been much less studied. In this study, we report the implementation of a TIRFM-based polarization technique to detect rapid submicrometer changes in plasma membrane topology as a result of exocytosis. The technique is based upon excitation of an oriented fluorescent membrane probe (the carbocyanine dye, diI) with a polarized evanescent field. DiI has been shown to embed in the membrane with its transition dipole moments nearly in the plane of the membrane (Axelrod, 1979). The technique in a nonimaging mode was pioneered by Thompson et al. (1984) to measure the orientational distribution of a probe (NPD-PE) incorporated within a model membrane. The technique was applied to time sequence imaging of dynamic orientational

Correspondence to Arun Anantharam: arunanan@umich.edu

Abbreviations used in this paper: CCD, charge-coupled device; Cer, cerulean; IDL, interactive data language; NPY, neuropeptide Y; p-pol, p-polarization; PSS, physiological salt solution; pTIRF, polarized TIRF; ROI, region of interest; s-pol, s-polarization; TIR, total internal reflection; TIRF, TIR fluorescence; TIRFM, TIRF microscopy.

The Rockefeller University Press $30.00
J. Cell Biol. Vol. 188 No. 3 415–428
www.jcb.org/cgi/doi/10.1083/jcb.200908010

changes in the plasma membrane itself on living cells labeled with diI (Sund et al., 1999). Recently, polarized TIRF (pTIRF) was used to demonstrate the spread of FM4-64 into the plasma membrane of PC12 cells (Taraska and Almers, 2004) and peptide-induced disorder in supported bilayers (Oreopoulos and Yip, 2009).

The technique involves taking successive images of a sample with orthogonal excitation polarizations in TIR mode: a p-polarization (p-pol; in the plane of incidence and perpendicular to the coverslip) and an s-polarization (s-pol; perpendicular to the plane of incidence and parallel to the coverslip) image. Regions, even submicroscopic ones, in which the membrane deviates from parallelism with the substrate are vividly highlighted by taking the ratio p-pol/s-pol (*P*/*S*) of the membrane-embedded diI fluorescence images excited by the two polarizations. This approach is generally applicable for visualizing dynamic topological alterations in the plasma membrane during important cellular processes.

In a theoretical section, we show which combination of p-pol and s-pol excited images reports the local fluorophore concentration independently of the orientation. We also examine the ability of pTIRF to highlight submicrometer morphological distortions in the plasma membrane in the presence of complicating factors including the finite evanescent field depth, near-field emission into the substrate, high aperture observation, membrane foreshortening, optical resolution limitation, and pixelation of the observation region.

In the experimental section, we describe high spatial and temporal resolution images of the granule membrane–plasma membrane complex in living bovine chromaffin cells taken as a repeated triplet sequence: p and s excitation of diI in the plasma membrane and also excitation (at a different wavelength) of the fluorescent protein–marked secretory granules. Guided by the theory section predictions, we demonstrate rapid and varied submicrometer changes in plasma membrane topology at sites of exocytosis that occur immediately upon fusion (within the time resolution of the imaging) and provide direct evidence for a persistent curvature in the exocytotic region after fusion that is subject to regulation. This occurs immediately upon fusion in at least 60% of events. The curvature decays with varying speeds from as fast as 450 ms to tens of seconds and is strongly affected by the dynamin GTPase inhibitor dynasore. Endocytosis was also imaged by optical techniques. We find that <10% of the fusion events stimulated with elevated K^+ result in rapid endocytosis. Thus, most of these topological changes are kinetically distinct from endocytosis and reflect a varying and regulated time course for the flattening of a fused granule membrane into the plasma membrane.

Results

Theory of polarized excitation TIRF

To help interpret our experimental results on the plasma membrane dynamics of secretion from chromaffin cells, we calculate the p-pol and s-pol excited image intensities for a particular geometrical model of secretion: a spherical membrane (the secretory granule) fusing with a planar membrane (the plasma membrane) from within the cell interior, taking into account several possibly countervailing optical effects.

Orientation versus concentration

Idealized geometry. In general, TIRF images show a convolved mix of local fluorophore orientations with concentrations and distances from the substrate. What combination of p-pol and s-pol excited images reports purely orientational distributions, and what combination reports purely concentration and distances?

To calculate the answer, we set up the following polar coordinate system (Fig. 1): the sample plane (at which TIR occurs) is the x-y plane, and the optical axis of the microscope is the z axis. The TIR evanescent field propagates in the x-y plane along x, s-pol excitation is polarized along y, and p-pol excitation is polarized along z (actually, a small amount of p-pol intensity is polarized in the x direction, dependent on the incidence angle of the TIR beam, but we will ignore it for simplicity). In this coordinate system, θ and ϕ are the polar angle (measured from the z axis) and the azimuthal angle (measured around the z axis), respectively.

For a particular fluorophore whose dipole is oriented in the θ and ϕ, the probability of excitation caused by p-pol or s-pol light is proportional to the square of the component of the dipole along the z or x axis, respectively. These square components are proportional to $\cos^2\theta$ and $\sin^2\theta\ \cos^2\phi$, respectively. Given that the fluorophore becomes excited, the emission can be resolved into two components, one along the z axis (i.e., perpendicular to the substrate) and the other in the x-y plane (i.e., parallel to the substrate). The square of each of these components, proportional to $\cos^2\theta$ and $\sin^2\theta$, each contribute to the emitted light that is collected by the objective with efficiencies $Q_\perp$ and $Q_\parallel$, respectively.

An actual sample, of course, contains numerous fluorophores with their dipoles possibly pointing in different directions. Assume that the normalized orientational distribution of dipoles is $\eta(\theta,\phi)$. The emission light intensities *P* and *S* gathered by an objective (and imaged at a single pixel) from p-pol and s-pol excitation, respectively, are

$$P = \int C\eta(\theta,\phi)\cos^2\theta\left(Q_\perp\cos^2\theta + Q_\parallel\sin^2\theta\right)\sin\theta d\theta d\phi$$
$$S = \int C\eta(\theta,\phi)\sin^2\theta\cos^2\phi\left(Q_\perp\cos^2\theta + Q_\parallel\sin^2\theta\right)\sin\theta d\theta d\phi, \quad (1)$$

where *C* is a number proportional to the local effective total amount of fluorophore at the pixel under view. *C* implicitly includes decaying effect of the evanescent field in the z direction such that fluorophores at larger distances from the surface simply contribute less toward *C*. *C* also implicitly includes the foreshortening effect of tangential viewing, all the multiplicative constants and efficiencies of absorption and emission that convert concentration into units of light intensity. The assumptions in Eq. (1) are that no polarizer is used in the emission system, the dichroic mirror introduces no polarization bias, the absorption and emission dipoles are parallel to each other, and

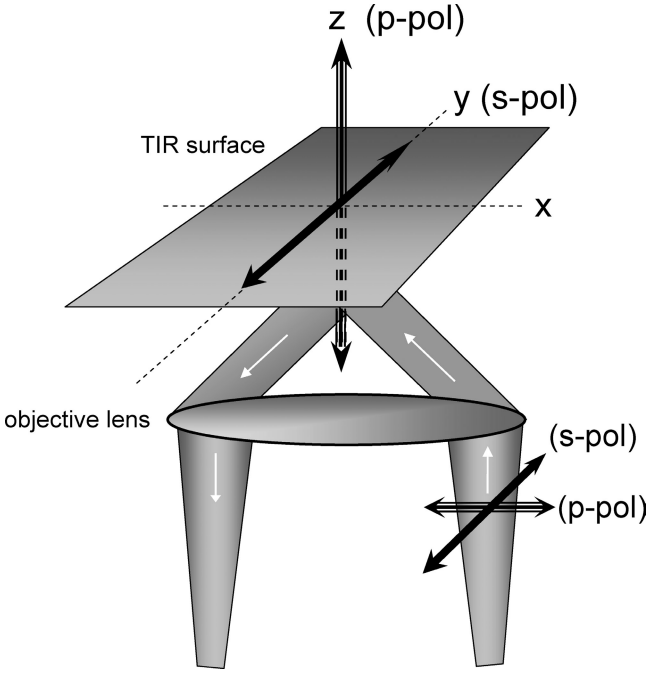

Figure 1. **Coordinate system.** The plane of incidence (which contains both the incident and reflected beams) is the x-z plane. The incident propagating beam (traveling up along z) is transversely polarized in either the x or y directions, which correspond to p-pol and s-pol, respectively. The evanescent field is polarized either primarily in the z direction (for p-pol) or entirely in the y direction (for s-pol).

the orientational distributions are not a function of z distance to the TIR substrate. Clearly, ratio *P/S* reports only upon the orientational distribution $\eta(\theta,\phi)$ because the *C* factors cancel upon taking the ratio. The goal of the following derivation is to find the opposite: a combination of *P* and *S* that only reports on *C* and does not depend on $\eta(\theta,\phi)$.

All of the possible biases of the objective toward gathering light from one excited dipole orientation or another are contained in the factors $Q_\perp$ and $Q_\parallel$. For a very high aperture (NA ≥1.40), these factors are within 20% of each other (see Materials and methods; Fig. 2 B), so we will set them both equal to unity in Eq. (1). This leads to collapse of the integrand factor involving $Q_\perp$ and $Q_\parallel$ to unity. Note that this step is valid only for 1.40, 1.45, and 1.49 NA objectives, and even then, it is just an approximation. The normalization requirement is that

$$\int \eta(\theta,\phi)\sin\theta d\theta d\phi = 1. \tag{2}$$

We now assume azimuthally symmetry in fluorophore orientation so that $\eta(\theta,\phi) = \eta(\theta)$; i.e., there is no particular orientation preference for ϕ in the x-y plane. This is expected to be the case in many biological organelles (plasma membrane, secretory granules, etc.) if we gather light from a large enough area. The normalization (Eq. 2) then becomes

$$\int \eta(\theta)\sin\theta d\theta = \frac{1}{2\pi}. \tag{3}$$

Then, Eq. (3) gives

$$P = \int C\eta(\theta)\cos^2\theta\sin\theta d\theta d\phi = 2\pi\int C\eta(\theta)\cos^2\theta\sin\theta d\theta$$

$$S = \int C\eta(\theta)\sin^2\theta\cos^2\phi\sin\theta d\theta d\phi = \pi\int C\eta(\theta)(1-\cos^2\theta)\sin\theta d\theta$$

$$= \pi C\int \eta(\theta)\sin\theta d\theta - \left(\frac{P}{2}\right) = \frac{C-P}{2}. \tag{4}$$

Therefore,

$$P + 2S = C.$$

This expression is true regardless of the exact form of orientational distribution $\eta(\theta)$ (as long as it is azimuthally symmetric). The sum *P+2S* is proportional only to the effective concentration. As long as we view with a very high aperture objective and bin together a large enough image area to ensure that the orientational distribution within the area is azimuthally symmetric, *P+2S* is approximately proportional only to the local concentration convolved with the evanescent exponential decay, and invariant with respect to the details of azimuthally symmetric orientation. Because $Q_\perp/Q_\parallel$ undulates as a function of z (Fig. 2), there is no algebraic combination of *P* and *S* that is exactly invariant to orientation for all geometrical shapes of the membrane.

We can plug in a particular azimuthally symmetric $\eta(\theta)$ function of interest here: the idealized cases of the fluorophore diI in a planar plasma membrane parallel to the substrate and on a spherical granule much smaller than the size over which *P* and *S* are evaluated. We assume for now that diI intercalates into lipid bilayer membranes with its dipole moments parallel to the local membrane surface (Axelrod, 1979). They are (in properly normalized form)

$$\eta(plane) = \left(\frac{1}{2\pi}\right)\delta\left(\theta - \pi/2\right)$$

$$\eta(sphere) = \left(\frac{1}{4\pi}\right),$$

where δ is the standard spike δ function. Using Eqs. 3 and 4 (with $C = 1$ for both plane and sphere, thereby implicitly assuming the same surface area for both) gives

$$\begin{aligned} P(plane) &= 0, \\ S(plane) &= 1/2, \\ P(sphere) &= 1/3, \\ S(sphere) &= 1/3. \end{aligned} \tag{5}$$

The ratio *P/S* changes from 0 to 1 in going from a pure plane to a pure sphere. This distinction provides a very sensitive test of local orientation. The sum *P+2S* remains constant at 1 and provides an orientationally independent means to measure relative local concentrations.

This idealized calculation must be altered to include numerous real effects: finite evanescent field depth, exocytotic structures containing both truncated spherical and planar regions, granule size on the edge of optical resolvability, and pixelation. These effects, and a general approach to handling them, are considered in detail in Materials and methods. Based

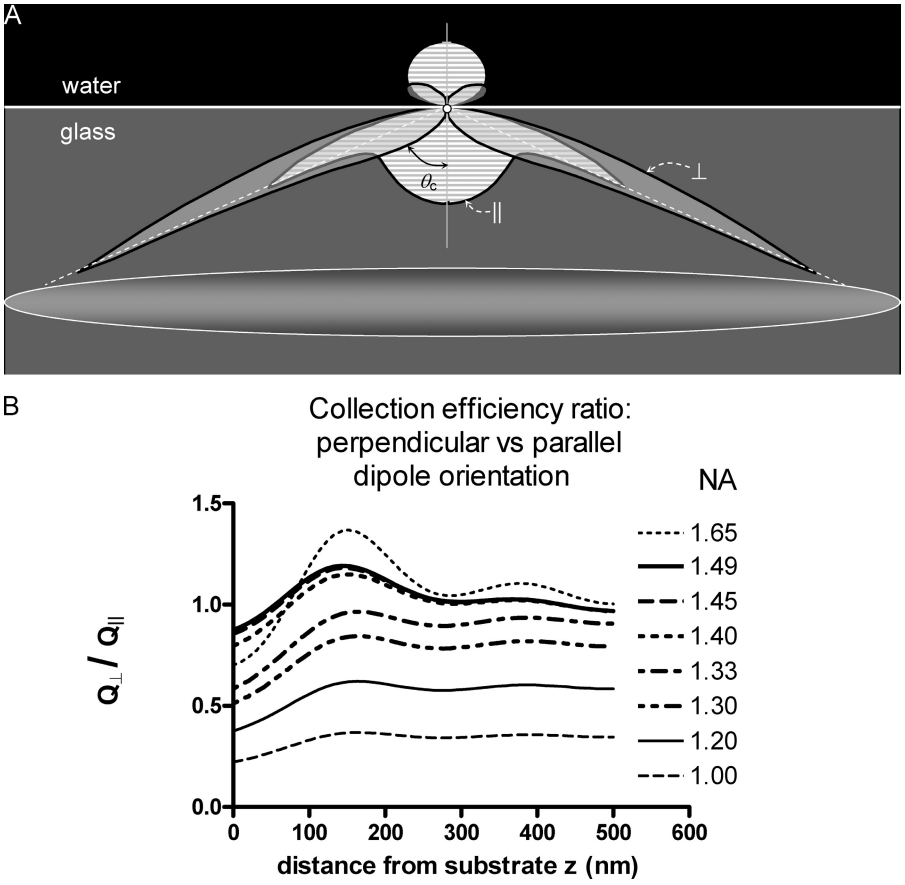

Figure 2. **Emissions from polarized excitations and the numerical aperture.** (A) Emission pattern from a fluorophore dipole located in water at z = 0 nm distance from a glass substrate. The fluorophore is shown as a small circle. The pattern is derived from the equations in Hellen and Axelrod (1987). The intensity into any polar angle is depicted as the radial distance from the dipole to the end of the shaded pattern; the gray horizontal stripe pattern and the uniform gray pattern indicates the emission from a dipole parallel and perpendicular to the surface, respectively. See Results for explanation. (B) Effect of objective NA on the collection efficiency for perpendicular and parallel dipole orientation. The relative amount of light captured from dipoles oriented parallel versus perpendicular to the substrate depends strongly on the objective NA and on distance z. These dependencies are shown in graphs of $Q_\perp/Q_{||}$ versus z for several different popular NAs. Objective-based TIR illumination requires an NA of at least 1.45; it is those objectives that show $Q_\perp/Q_{||}$ close to unity, with some undulations as a function of z. The 1.49 NA shows the smallest deviation from unity over the whole range of z distances and allows the conclusion that *P+2S* is a fairly good measure of total concentration. The 1.65 NA must use refractive index 1.78 (rather than 1.52) coverslip and oil, so the distortion of the emission pattern (as a result of near-field capture) is the strongest for that objective.

on those considerations, computer-simulated images (Fig. 3) and expected integrated intensities for *P* and *S* (Fig. 4) can be produced.

The range of *P*/*S* predictions derived from this realistic image simulation (with parameters specified in Fig. 4 A) agree with the range of experimentally observed *P*/*S* values on bovine chromaffin cells (see Test of theory on…). The agreement does not mean that the actual indentations are truncated spheres, but it does suggest that the actual indentations are quite significant. The solid and dashed lines in the *P*/*S* graphs of Fig. 4 A correspond to different granule radii, 150 and 250 nm. For a constant-sized, pixelated region of integration, the *P*/*S* ratio reaches a greater maximum for larger granules in the course of fusion with the plasma membrane.

Fig. 4 B shows that *P+2S* is rather insensitive to the depth of indentation until the indentation is beyond a hemisphere. Therefore, any large changes in *P+2S* indicate either (a) a deep indentation, (b) an actual increase in fluorophore concentration, or (c) a different geometry than assumed by the sphere/planar model. Large granules (radius [R] = 250 nm) do show a decrease in *P+2S* in the middle of the indentation depth range, as the simulated image develops a larger dark hole at its center.

Test of theory on model systems

According to the idealized theory (Eq. 5), the *P*/*S* ratio should equal 0 if the diI transition dipoles are parallel to the membrane and the membrane is parallel to the coverslip substrate. This prediction was tested with HEK293 cells stained with diI. The plasma membrane was imaged with p- and s-polarized 514-nm excitation. The *P*/*S* ratio of the plasma membrane apposed to the glass coverslip was not uniform. The minimum *P*/*S* ratio was 0.304 ± 0.017 (n = 6 cells) and was assumed to represent areas parallel to the coverslip. This value could be greater than zero for several reasons. (a) The absorption and/or emission dipoles of diI are not parallel to the bilayer but are at a somewhat oblique angle. A *P*/*S* ratio of 0.3 is predicted for if the transition dipoles are oriented an angle β of 69 rather than 90° from the normal to the bilayer. This value for β was used to generate the curves shown in Fig. 4. (b) The p-pol evanescent field is not purely perpendicular to the glass interface but in reality is elliptically polarized in the x-z plane with a weak x component (Axelrod, 2001) of ∼6.8% of the total p-intensity at the incidence angle used in this study. This x component would cause a deviation of *P*/*S* from zero but not nearly accounting for a *P*/*S* of 0.3 and was not considered in the calculations. (c) The evanescent field obtained with through the lens TIRFM is contaminated by impurely polarized propagated light because of internal reflections in the objective (Mattheyses and Axelrod, 2006). The impurity accounts for ∼10% of the total intensity at the substrate surface and increasing amounts further into the aqueous phase but was not considered in the calculations. (d) The diI absorption and emission dipole moments are not totally parallel to each other, as discussed in Axelrod (1979). However, because the 1.49 NA objective is relatively insensitive to the orientation of the emission dipole, this nonparallelism probably has little effect.

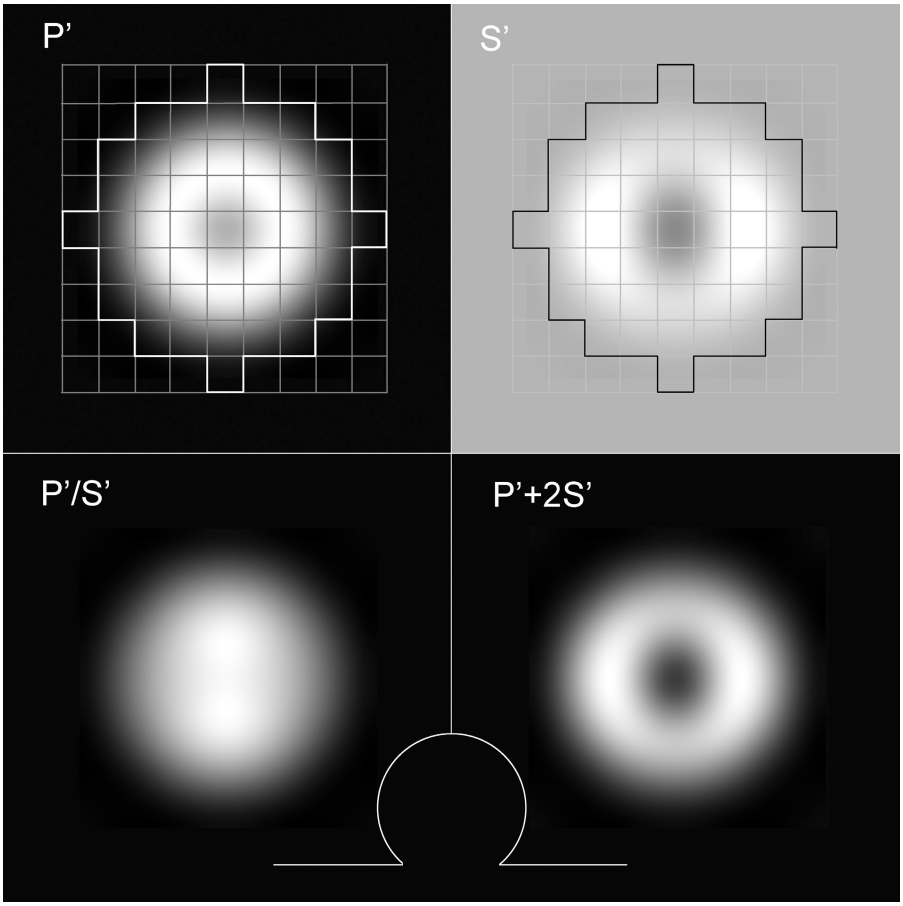

Figure 3. **Simulated Images.** Based on Eq. 6 and a custom IDL program, the expected intensity patterns *P′* and *S′* for p-pol and s-pol excitation, respectively, are shown for a dil-labeled spherical granule fusing with (and truncated by) a dil-labeled planar plasma membrane. In this particular simulation, most of the sphere is still intact; only the lower one fourth of its radius is truncated off. The schematic line drawing (white) shows a side view of this configuration at the same scale as the simulated images. The effects of finite evanescent depth, optical resolution limit, and nonparallelism of the dil dipole with the membrane are all included in generating these *P′* and *S′* patterns, thereby simulating what appears at the CCD array image plane. The pixelation of the CCD array is superimposed along with an outline showing which pixels are actually used to integrate the total intensities *P* and *S*. The ratio *P′/S′* and the sum *P′+2S′* are also shown. The corresponding pixel by pixel ratios and sums on experimental data (as pixelated by the camera) are used to determine lateral positions of dil/membrane morphology features at the time of exocytosis. However, extended temporal tracking of the p-pol and s-pol ratios and sums uses the spatially integrated values *P* and *S* (without the primes) before forming the *P/S* and *P+2S* combinations. The predictions of the simulations are sensitive to the assumed parameters, which are set close to the actual or expected experimental values: granule radius = 150 nm; Airy disk half-width (out to first minimum) = 211 nm; evanescent field depth = 110 nm; side length of CCD array pixel (as projected onto the image) = 73 nm; angle β between membrane normal and dil dipole = 69°. The *P′* and *S′* images are shown with the same grayscale; the *P′/S′* and *P′+2S′* each have their own gray scales.

Eq. 5 also predicts a *P/S* equal to 1 for an isotropic distribution of fluorophore dipoles. This distribution was approximated by diI-labeled beads. The beads gave a *P/S* ratio of 0.890 ± 0.042 (n = 21), much larger than for the planar membrane on HEK cells and only slightly less than the theoretical value of 1.0. The quantitative discrepancy from theory can be explained. The bead sample does not really qualify as an isotropic distribution of diI; the beads are on the same order of size as the evanescent field depth and are thereby illuminated nonuniformly, with the part closest to the substrate (the part presumably with a small *P/S* ratio) contributing the most to the fluorescence intensity.

In summary, emissions obtained with p- and s-polarized excitations with diI in defined geometries are similar to the predictions of the theory. Most importantly, the *P/S* ratio is much greater (threefold) for diI on a spherical bead compared with diI in a bilayer parallel to the coverslip.

pTIRFM detects topological changes of the plasma membrane at sites of exocytosis

Chromaffin cells were transfected with neuropeptide Y (NPY)–cerulean (Cer) to label secretory granules and subsequently stained with diI immediately before imaging. As discussed in Materials and methods, a sequence of three images (NPY-Cer, s-polarized diI, and p-polarized diI) was acquired. The footprint of a chromaffin cell is predominantly parallel to the glass coverslip as indicated by the emission from s- being much brighter than from p-pol over most of the cell surface (Fig. S2).

The granule membrane becomes continuous with the plasma membrane upon exocytosis, allowing diffusion of the diI from the plasma into the granule membrane. A high K^+ (56 mM) depolarizing solution was perfused locally on the cell of interest to stimulate exocytosis. A short-lived local change in orientation of the diI-labeled membrane occurs around the time of exocytosis (Fig. 5). Fig. 5 A (top) shows a series of NPY-Cer images acquired at the indicated times. Time 0 represents the frame sequence just before exocytosis (i.e., the last frame before disappearance of the NPY-Cer–labeled granule). The corresponding *P/S* and *P+2S* images of diI-labeled membrane are also shown (Fig. 5 B, bottom). The *P/S* ratio increased locally within 260 nm of the last location of the granule immediately after release of NPY-Cer (see Fig. 9 A). The mean *P/S* ratio in a 292-nm radius region of interest (ROI) centered on the *P/S* spot increased 20% in the frame after fusion (Fig. 5 B, dotted lines) and declined back to baseline within 40 s.

A brief dimming in the *P+2S* image within the circled region was also visible, which is consistent with a decrease in

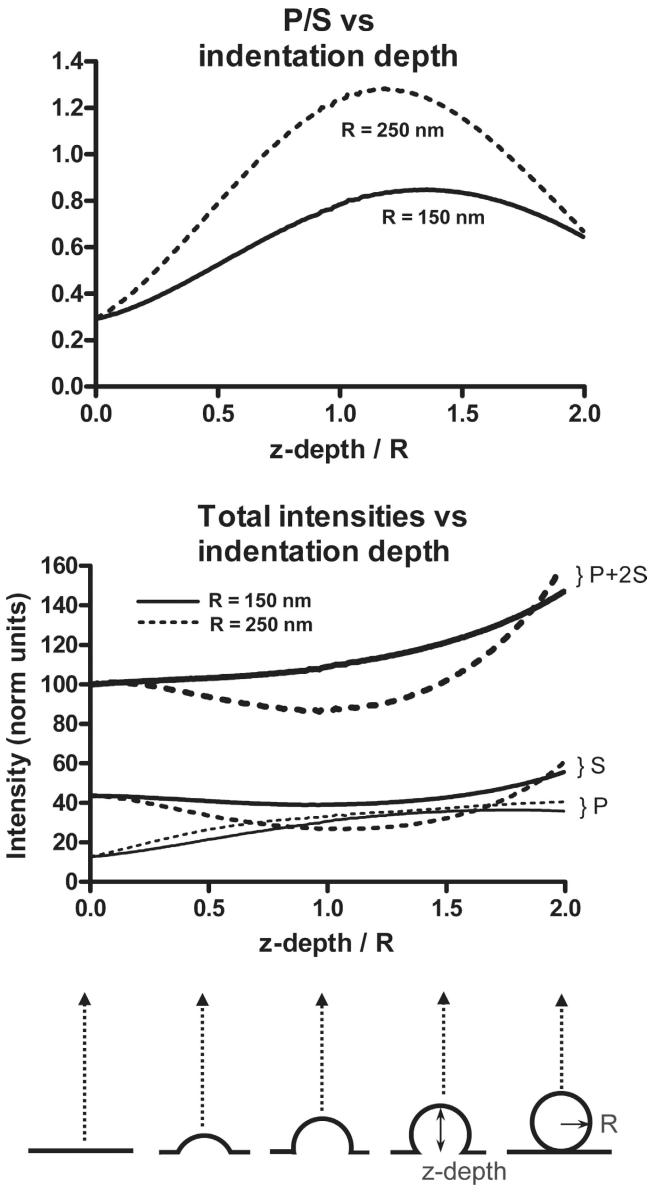

Figure 4. **Simulated P/S and *P+2S* as a function of spherical indentation depth z_d.** The geometry of the indentation structure is schematically shown at the bottom. The individual *P* and *S* intensities are also shown. The exact $Q_{\perp}$ versus z and $Q_{||}$ versus z collection efficiencies, as calculated from Hellen and Axelrod (1987) for NA = 1.49, were used to generate these curves. Parameters assumed in the simulation are R = 150 nm (solid) or 250 nm (dashed) radius spherical indentation, dil labeling in both the indentation and planar areas, convolution with a point-spread function of half-width 211 nm to simulate the optical resolution limit, an evanescent field e^{-1} depth of 110 nm, an angle β between dil dipoles and the normal to the plane of the membrane of 69° (see Test of theory…), and a distance between the TIR substrate and the planar parts of the structure of 50 nm. Images generated with these parameters are then pixelated in simulation with a pixel size of 73 nm. Only those pixels whose centers fall with a radius of 4-pixel widths (292 nm) from the center of the image are counted toward total intensities *P* and *S*. The values for *P* and *S* that would be expected from a completely flat membrane are seen as the ordinate intercepts at $z_d/R = 0$. The curves are changed only slightly if the collection efficiencies $Q_{\perp}$ and $Q_{||}$ are equal at all z positions.

the local concentration of diI and/or movement of membrane away into the cell (Fig. 5, A and B). The *P+2S* emission subsequently returns to baseline.

The cartoon (Fig. 5 C) depicts an interpretation of these measurements. Immediately upon fusion, the granule membrane retains its curvature, and diI rapidly diffuses into the fused granule membrane. Indeed, it has been shown in PC12 cells that within 30 ms of fusion, lipid diffusion is not significantly restricted between the granule and plasma membrane (Taraska and Almers, 2004). The *P/S* ratio increases because of the curvature; the *P+2S* emission decreases because the granule membrane is recessed from the surrounding plasma membrane. Subsequently, the fused granule–plasma membrane complex flattens over time. The theoretical analysis indicates that because of the limit of resolution, the ability to detect a decrease in emission because of a fused and recessed granule membrane is dependent on the size of the fusing granule. A granule of 150-nm radius, just under the median granule radius 175 nm (Coupland, 1968), would show no decrease in *P+2S* (Fig. 4) during fusion. However, a granule of >250-nm radius could result in a measurable decrease in *P+2S* during fusion. Indeed, granules of this size or larger account for 15% of the epinephrine-containing granules in bovine adrenal chromaffin cells (Coupland, 1968).

There is variety in both the magnitude and duration of the local *P/S* and *P+2S* changes detected upon exocytosis (Fig. S3). This is likely to reflect differences in both the initial topology of the fused granule–plasma membrane complex upon exocytosis and its subsequent fate (e.g., flattening of the complex into the plasma membrane or endocytosis). The responses of the membrane to fusion are summarized in a cumulative frequency histogram (Fig. 6 A, control). The dotted vertical line at 6% *P/S* change indicates the level above which the ratio is significant (see Materials and methods). The *P/S* ratio increased significantly in 60% of the events ($n = 50$) within 0.45 s of fusion. Fusions without evident changes in *P/S* may reflect transient topological changes that occurred faster than the temporal resolution of the technique. Indeed, preliminary data with a faster image acquisition rate of 10 Hz suggests that ~80% of fusion events are associated with an increase in *P/S*. When the *P/S* does increase with fusion, there is a tendency for it to subsequently decline (Fig. 6 B). For example, after 31.5 s, 70% of the events had declined to baseline (Fig. 6 B).

P+2S measurements (proportional to the total diI convoluted with membrane position in the evanescent field) were aligned to the frame immediately before fusion and averaged for fusion events that had significant changes in *P/S* (Fig. 6 C, control). Superimposed on a gradual decline of *P+2S* that reflects photobleaching was an immediate but transient dip (Fig. 6 C, arrow) immediately after fusion. This dip probably reflects the occasional occurrence of a diI-labeled granule membrane that remains recessed after fusion (Fig. 5).

Topological changes are temporally distinct from endocytosis

Rapid topological changes immediately after fusion could reflect rapid endocytosis. However, the following experiments indicate that rapid endocytosis is a relatively rare event during elevated K^+ stimulation and can only account for a small fraction of topological events after fusion.

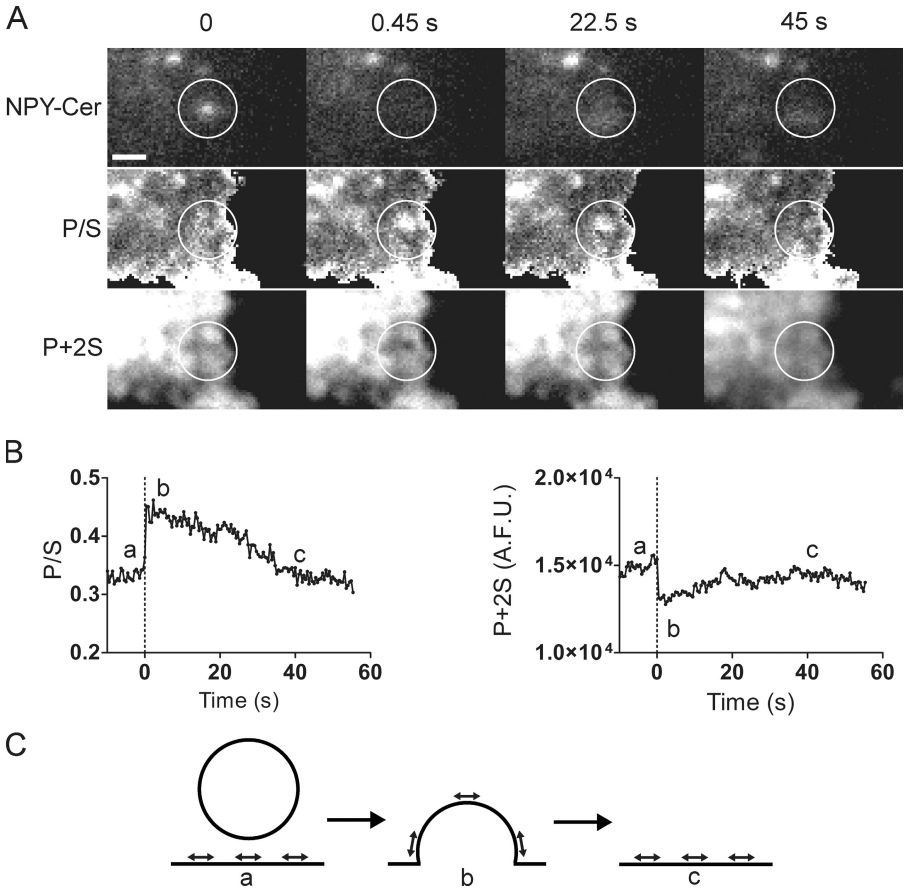

Figure 5. **Changes in the topology of the plasma membrane at sites of exocytosis.** (A) *P/S* and *P+2S* images were calculated and aligned to the NPY-Cer image at the times indicated. An NPY-Cer–labeled granule undergoes exocytosis between time 0 and 0.45 s. An increase in pixel intensity in the approximate location of the NPY-Cer image stack is observed, which is consistent with a change in orientation of membrane-intercalated dil (there is a 254-nm offset between the center of mass of the NPY-Cer granule and *P/S* spot; Fig. 9). In the *P+2S* image, a dimming is observed. Circles are centered over the last observed location of the granule. Bar, 1 µm. (B) Membrane *P/S* and *P+2S* were followed for almost 60 s. The dotted line at time 0 indicates the frame before fusion (i.e., the last frame in which the NPY-Cer granule was clearly visible). (C) One possible interpretation of the results in A and B are considered. DiI transition dipole moment orientation is indicated by direction of arrows.

The relationship between the fusion-induced topological changes and endocytosis was investigated with vesicular monoamine transporter 2–pHluorin (VMAT2-pHL). VMAT2 is normally present on bovine chromaffin granules and mediates the transport of catecholamine into the granule. Transfected VMAT2 is punctate with 80% colocalization with endogenous dopamine β-hydroxylase, a marker for the granule (Wick et al., 1997). The chromophore in VMAT-pHL is lumenal and normally quenched by the low lumenal, pH 5.5 (Holz et al., 1983). We found that upon fusion, the VMAT2-pHL gives a bright punctate spot (Fig. 7 A) that often lasts for tens of seconds with some diffusion away from the fusion site. To detect endocytosis, the pH of the extracellular solution was repeatedly changed every 10 s between 7.4 and 5.5 (MES buffer substituted for Hepes; Ferguson et al., 2007). Bafilomycin was present (unless otherwise indicated) to inhibit reacidification of granules that underwent endocytosis (Fernández-Alfonso and Ryan, 2004).

The low extracellular pH quenches surface pHluorin but not pHluorin that had undergone endocytosis as shown in Fig. 7 A. Single endocytotic events were readily detected (two events; Fig. 7 A, circles and arrows). Less than 10% of fusion events were associated with rapid endocytosis in control cells (Fig. 7 B). It is unlikely that there were additional events that the method failed to detect as a result of insufficient VMAT2-pHL because granules with the most VMAT2-pHL were not preferentially detected (Fig. 7 C). Because at least 60% of the fusion events showed distinct topological changes upon fusion, most of them do not correspond to rapid endocytosis. In fact, endocytosis would be predicted to result in an increase in *P+2S* (as well as in *P/S*; Fig. 4 B, right), an event that has almost never been observed in control cells (Fig. 6 C and Fig. S4). Thus, the topological changes occurring immediately after exocytosis most likely reflect a varying time course of fusion pore widening and flattening of the granule membrane into the plasma membrane.

Endocytosis could not be detected in the absence of bafilomycin (Fig. 7 B), indicating that acidification normally occurs within seconds. This finding indicates that endocytic vesicles that form at the sites of exocytosis of dense core granules in chromaffin cells are likely to be able to take up catecholamine soon after formation. Acidified vesicles may sequester catecholamine that enters the cell through the plasma membrane catecholamine transporter after release.

Topological changes upon exocytosis are regulated by dynamin

Dynamin not only plays an important role in clathrin-dependent and -independent endocytosis but has also been implicated in the regulation of protein release from secretory granules (Tsuboi et al., 2004). Dynamin also tubulates lipid membranes in vitro (Sweitzer and Hinshaw, 1998), raising the possibility that its membrane-shaping function regulates the topology of the granule–plasma membrane complex after fusion.

The role of dynamin in the local topological changes after fusion was investigated by inhibiting the GTPase activities of

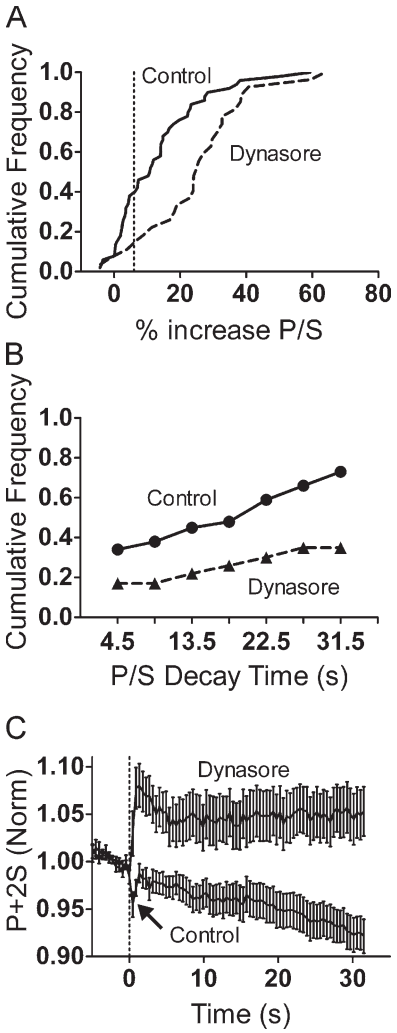

Figure 6. **The magnitude and duration of P/S and *P+2S* changes at the sites of fusion differ in control and dynasore-treated cells.** (A) A cumulative frequency histogram was generated to compare the frequency and magnitude of *P/S* changes observed with fusion in control (50 granules) and dynasore (27 granules)-treated cells. A greater fraction of fusion events show an associated increase in *P/S* with dynasore. The percent increase was calculated by taking the difference between the *P/S* at a particular frame $(P/S)_f$ and the mean *P/S* of 10 prefusion frames (Ave_{pre}) divided by the mean; $[(P/S)_f - Ave_{pre}]/Ave_{pre}$. The two histograms are significantly different ($P < 0.05$ by Mann-Whitney test). (B) The decay of the initial increase in *P/S* after granule fusion was followed. Only those events that showed an increase of at least 6% in *P/S* (compared with the prefusion baseline) in the first 0.45 s after fusion and that could be followed for 31.5 s after fusion were considered (control, $n = 29$; dynasore, $n = 25$). The fraction of events with a *P/S* increase that subsequently declines to the baseline within 4.5, 9, 13.5, 18, 22.5, 27, and 31.5 s are plotted for the two conditions. (C) The *P+2S* of fusion events with a significant increase in *P/S* were aligned to their prefusion frames and averaged (control, $n = 29$; dynasore, $n = 25$). The data were also normalized to the mean of 10 prefusion frames. The arrow indicates a transient dip in *P+2S* in control cells. In dynasore-treated cells, an increase in *P+2S* is usually observed. The two datasets are significantly different at every point after time 0 ($P < 0.05$ by Student's unpaired *t* test). Numbers are presented ± SEM.

dynamin with dynasore (Macia et al., 2006). Dynasore is a membrane-permeant inhibitor of dynamin 1 and dynamin 2, both of which are expressed in chromaffin cells. A brief preincubation with dynasore caused significant changes in the topological responses that follow exocytosis. An example of a typical response is shown in Fig. 8. *P/S* immediately increased after fusion then decreased somewhat but remained elevated for tens of seconds. Most remarkably, *P+2S* increased, a response that is rarely observed in control cells (Fig. S4).

The topological changes in the presence of dynasore and controls are summarized and compared in Fig. 6. *P/S* changes in the presence of dynasore tended to be larger (Fig. 6 A), with a greater fraction of fusion events in the presence of dynasore associated with an immediate increase in *P/S* (86% dynasore and 60% control; Fig. 6 A,). Moreover, *P/S* increases decayed more slowly to baseline in the presence of dynasore (Fig. 6 B). For example, by 31.5 s, 70% of the *P/S* changes in the control but only 35% in the presence of dynasore had returned to baseline. Most dramatically, *P+2S* tended to increase after fusion and stay elevated for tens of seconds (Fig. 6 C). Significant increases in *P+2S* occurred in 14 of 25 events (56%) in which *P/S* was elevated in the presence of dynasore but in only 1 of 29 events (3%) in control (Fig. S4).

The increase in *P+2S* strongly suggests that there is more diI-labeled membrane at the site of fusion, which is consistent with superimposed curvature from the fused granule and flat plasma membrane. A likely structure is a fused granule membrane that retains curvature ($R > 1.0$; Fig. 4; and Fig. 8 C, b). *P+2S* tended to undergo photobleaching in control but much less so for events in the presence of dynasore. This is also consistent for the structure proposed in Fig. 8 B (b) because a significant amount of the diI is subject to lower intensity excitation because of the decaying evanescent field in the unflattened granule membrane compared with the plasma membrane. DiI molecules in the fused but recessed granule membrane would be exposed on average to one third the excitation intensity compared with diI in the plasma membrane (Schmoranzer et al., 2000).

Electron microscopy indicates that the inhibition of dynamin GTPase activity by dynasore arrests clathrin-mediated endocytosis with clathrin-coated structures that have connections to the plasma membrane with narrow or broad necks (Macia et al., 2006; Newton et al., 2006). The imaging of the topological changes after fusion suggests that dynasore causes the formation of similar structures within 0.5 s of fusion.

Lateral displacement of localized topological change in plasma membrane and the last granule position before fusion

Postfusion increases in *P/S* occurred close to the last position of the granule before fusion, but they were often not overlapping. A striking example of this lateral displacement is shown in Fig. 9 A and Fig. 5 A. There was a 254-nm displacement from the center of the solid white circle (last position of granule before fusion) to the center of the dashed white circle (position of increased *P/S*). We determined the lateral displacements for fusion events in which there was a clear increase in *P/S* using a center of mass calculation as described in Materials and methods (Fig. 9 B). The mean displacement of the *P/S* change from the last position of the granule was 122 ± 15 nm. Such displacements are consistent with the finding that granules move tens to hundreds of nanometers within 100 ms of fusion (Allersma et al., 2006; Degtyar et al., 2007).

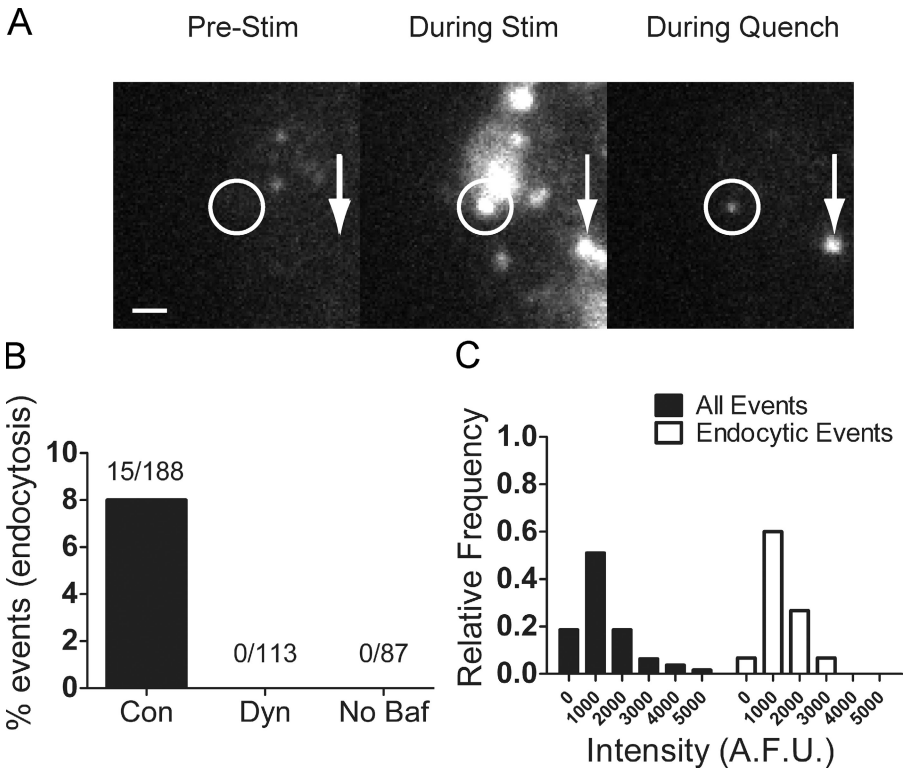

Figure 7. **Endocytosis at the site of fusion is infrequently observed.** Chromaffin cells expressing VMAT-2 pHluorin were exposed to cycles of low, pH 5.5, and high, pH 7.4, every 10 s after an initial 15-s stimulation with 56 mM K^+ in the presence of bafilomycin. (A) Two bright puncta (fusion events) that appear during stimulation are highlighted (circle and arrow). These events are subsequently insensitive to low pH exposure (quench) within 25 (circle) and 10 s (arrow). Bar, 1 µm. (B) Low pH-insensitive events (endocytic events) expressed as a percentage of total fusion events observed. (C) The initial intensity of all fusion events compared with the intensity of only the events that subsequently showed rapid endocytosis.

Discussion

In previous studies, we and others have investigated granule motions that immediately precede fusion but without concomitant high spatial and temporal resolution of localized plasma membrane topology. In this study, using a combination of dual labeling and pTIRFM, we have succeeded in visualizing fusion by imaging the release of granule contents and the accompanying changes in the local plasma membrane topology. We have extended the theory of pTIRF for measurement of membrane topology, taking into account the emissions captured by a high NA objective and have predicted the emissions from topological changes anticipated in exocytosis. Experimentally, we have demonstrated with high spatial and temporal resolution imaging of plasma membrane diI with p-TIRFM that the technique is able to capture rapid and varied submicrometer changes in topology at sites of exocytosis in chromaffin cells.

The approach used in the theoretical development of pTIRF and the computer simulations should be generally useful in a wide range of studies of plasma membrane morphological dynamics. We show how, under a set of common assumptions and optical conditions, the ratio *P/S* reports purely upon local membrane orientation, and the linear combination *P+2S* reports purely on local concentrations (convolved with distance to the glass coverslip). For a model of the membrane geometry of exocytosis (a spherical shell truncated by and fusing with a plane), we have derived the expected *P/S* and *P+2S* measures, taking into account many practical factors: granule radius, evanescent field depth, optical resolution limitation, size of integration area, and detector pixelation. Although it is intuitively expected that *P/S* should increase whenever the membrane is nonparallel with the substrate, many of the considered factors work in opposite directions so the amplitude of the increase is not easily anticipated. In the case of *P+2S*, the theoretical results are also complicated: some geometries and optical setups can lead to an increase and others to a decrease. Nonetheless, an appropriate model can provide the basis for a reasonable and reliable interpretation of the experimental results.

Direct visualization of fusion pore expansion

Recent work supports the idea that events associated with the fusion pore can take distinct pathways. This has important implications for the extent to which plasma membrane morphology is reordered upon fusion. The classical pathway or model holds that subsequent to fusion pore formation, granules merge completely with and flatten into the plasma membrane. Some granule membrane constituents can diffuse away. The granule lipid and some of its proteins are internalized, and the granule membrane rebuilt through poorly understood intracellular sorting mechanisms (Winkler, 1977). Soluble protein content is likely added during interaction with the Golgi. This pathway may be preferred after intense stimulation in chromaffin cells (Fulop et al., 2005). In the second pathway of fusion/recycling, a fusion pore is also formed through which some or all of the granule cargo is released. However, the pore is not fully expanded as in the classical model but rather is closed after a variable amount of time. Thus, the granule does not collapse fully into the plasma membrane, and the empty or nearly empty granule cavity is recaptured largely intact (Taraska et al., 2003; Tsuboi and Rutter, 2003; Perrais et al., 2004; Tsuboi et al., 2004; Fulop et al., 2005). This model has been termed granule cavity recapture or "cavicapture" (Henkel and Almers, 1996).

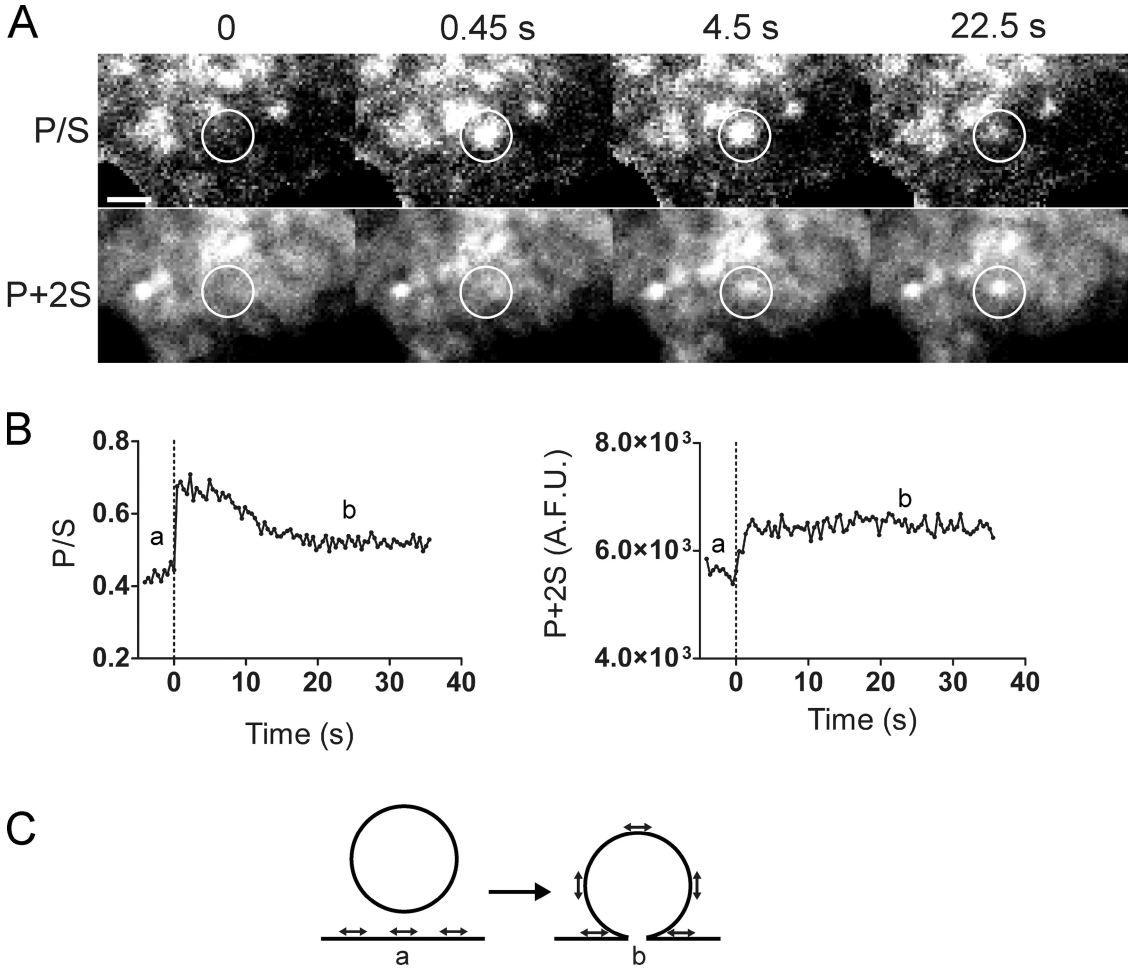

Figure 8. **Plasma membrane topological changes become long lived in the presence of dynasore.** Dynasore was added to the bathing solution at a final concentration of 80 µM at least 10 min before the imaging. (A) Long-lived increases in *P/S* and *P+2S* are observed after fusion of a granule (release of NPY-Cer). Circles are centered over the last observed location of the granule. Bar, 1 µm. (B) Data from A is presented with the vertical dotted line indicating the frame before fusion. (C) Schematic interpretation of the event in A. In the presence of dynasore, a fused structure is formed with significant indentation and curvature that is connected to the plasma membrane.

Another possibility is that the granule fuses with the plasma membrane and only partially flattens into the plasma membrane, retaining curvature without immediate endocytosis. This type of behavior has been observed after fusion of cortical granules in sea urchin eggs (Terasaki, 1995). The fate of the granule membrane immediately upon exocytosis in mammalian cells has been indirectly surmised but has been difficult to directly image because of the small size of the granules and the rapidity of the events.

In this study, pTIRFM was adapted to monitor the transient changes in the plasma membrane upon exocytosis in chromaffin cells. Upon exocytosis (sudden release of NPY-Cer), there was an immediate and significant localized increase in the *P/S* ratio in >60% of the events. Recent, higher frequency imaging indicates that ∼80% of the fusion events have significant increases in *P/S*. The increase in *P/S* likely reflects the union of the granule and plasma membranes with this new entity retaining some of the granule curvature. The topological changes decay with a varying time course from less than a second to many tens of seconds, probably representing different outcomes after the initial fusion event.

One possible outcome for the granule membrane after fusion is recycling by rapid endocytosis. This process occurs within hundreds of milliseconds to seconds after fusion, is regulated by dynamin 1, and is independent of clathrin (Artalejo et al., 2002; Fulop et al., 2008). The electrophysiological approaches that have studied this process were not designed to localize individual exocytotic and endocytotic sites in real time. In this study, individual exocytotic and (rapid) endocytosis events were imaged with VMAT2-pHL. Only ∼10% of the fusion events were associated with endocytosis within 30 s of fusion. Because at least 60% of the fusion events showed distinct topological changes upon fusion, the changes do not correspond to rapid endocytosis. They likely reflect a varying time course of fusion pore widening and flattening of the granule membrane into the plasma membrane. The fused granule membrane sometimes flattens into the plasma membrane in less than a second but often retains curvature for tens of seconds.

We also routinely detected less than a one–granule diameter shift between the last observed position of the granule and the topological change. This provides further evidence for granule motion in the moments just before the fusion event (Allersma et al., 2006; Degtyar et al., 2007).

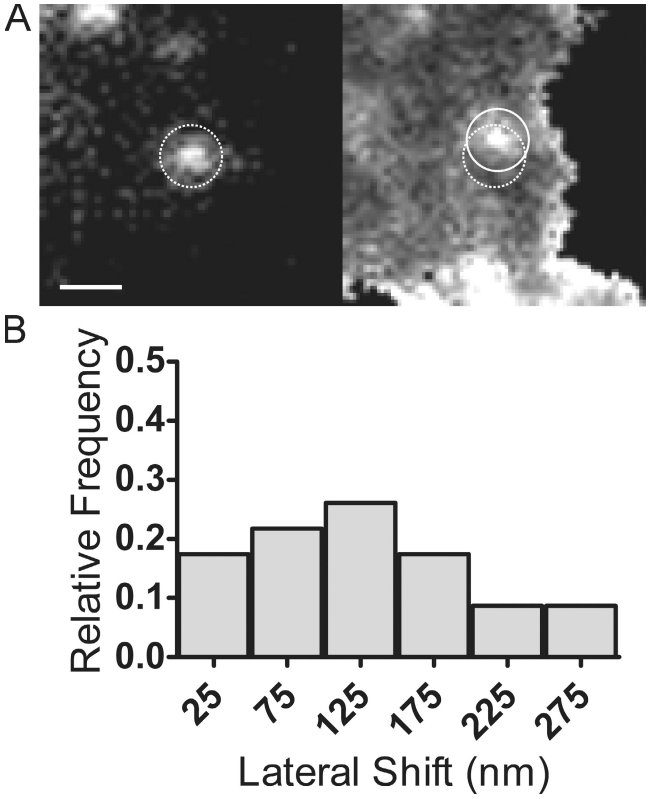

Figure 9. **Lateral displacement of localized topological change in plasma membrane and the last granule position before fusion.** (A, left) A dashed circle is centered on the last observed position of a fusing granule. (right) A solid circle is centered on the first observed location of a *P/S* spot. Bar, 800 nm. (B) The lateral displacement from the center of mass of the fusing granule to the center of mass of the *P/S* puncta for 23 fusion events is plotted in a frequency histogram. The mean displacement observed was 122 ± 15 nm.

Topological changes detected by pTIRF are modulated by inhibition of dynamin GTPase activity

Experiments with dynasore suggest that dynamin plays a role in determining the topological outcome of exocytosis. This specific inhibitor of the dynamin GTPase caused qualitative changes in the topological responses that suggest stabilization of a postfusion intermediate of a granule connected to the plasma membrane. This intermediate was rarely detected in the absence of dynasore but occurred in >50% of the topological changes in the presence of dynasore. A function for dynamin immediately upon fusion had been suspected from a variety of experiments that measured the release of granule contents (Graham et al., 2002; Tsuboi et al., 2004; Fulop et al., 2008) and membrane proteins (Jaiswal et al., 2009). However, it is not possible to say at this time whether the alterations in membrane topology detected with dynasore are due solely to dynamin inhibition or to a secondary effect such as clathrin stabilization at the plasma membrane.

Summary

We have shown that pTIRF can be understood theoretically and can be implemented in a manner that should have wide applicability for the study of biological processes that involve plasma membrane shape changes and deformations. We visualize for the first time topological features of the expanding fusion pore, provide evidence that its dynamics are regulated by dynamin, and distinguish the topological changes from rapid endocytosis. The experiments support the notion that the granule membrane and plasma membrane become a unique entity upon fusion whose dynamics and function are specifically regulated.

Materials and methods

Theoretical details: NA effects

The emission pattern of a dipole near a surface is rather complex, with both the intensity and polarization as a function of both the observation angle and the fluorophore orientation. A microscope objective, which gathers light over a wide range of observation angles, will thereby see an intensity and polarization that is a strong function of its NA. Aspects of the relevant classical physical optics theory have been worked out by several groups of researchers, notably by Burghardt and Thompson (1984), who examined how much fluorescence is captured by a nearby microscope objective from a fluorophore in a dielectric material sandwiched between two other (possibly different) dielectric materials. Using the same general approach but with some modifications, Hellen and Axelrod (1987) calculated the emission intensity patterns from a fluorophore located in, e.g., water at or near a glass substrate interface possibly coated with an intermediate material. The graphical results and discussion in this study are developed from digital integration of the relevant equations in Hellen and Axelrod (1987).

The emission intensity patterns can be graphically shown on a polar plot (Fig. 2 A). The emission intensity in any particular direction is denoted by the radial distance from the center, at which a fluorophore is located (Fig. 2 A, small circle). Two patterns are shown: one produced by an excited fluorophore with its dipole oriented parallel to the surface (Fig. 2 A, thicker line) averaged over all azimuthal angles; the other with its dipole oriented perpendicular to the surface. Note that the perpendicular dipole emits very little light end-on along the z axis toward the objective (out of view below). Both orientations produce sharp intensity peaks at an angle corresponding to the critical angle. Both orientations also emit light into the glass at angles greater than the critical angle, but the intensity at these supercritical angles drops to zero at an observation angle skimming along the interface. The supercritical intensity is due entirely to the interaction of the dipole's near field (a nonpropagating component of the dipole field, strongest within a wavelength of the fluorophore) with the surface. For objectives with a small NA, fluorescence from parallel dipole clearly dominates. For larger NA, fluorescence from a perpendicular dipole becomes increasingly important.

Fig. 2 A assumes that the dipole resides right upon the surface (z = 0). For dipoles a little farther out into the solution, the intensity pattern changes as the dipole's near field interacts less with the surface. The pattern also changes somewhat because reflection of emitted light off the surface gives rise to interference effects. The collection efficiency (proportional to the amount of light collected by an objective) for each dipole thereby depends on z. The collection efficiency is denoted as $Q_{\perp}$ and $Q_{||}$ for perpendicular and parallel dipoles, respectively.

Fig. 2 B shows the ratio of $Q_{\perp}/Q_{||}$ as a function distance of the dipole from the surface (in nanometers) for a selection of different NAs. $Q_{\perp}/Q_{||}$ increases with increasing NA as expected. For 1.49 NA objectives, $Q_{\perp}/Q_{||}$ is fairly close to 1 (actually 1.0 ± 0.2, depending on the fluorophore's distance from the surface). Therefore, 1.49 NA objectives see both parallel and perpendicular excited fluorophore dipoles (roughly) equally well; they don't care what the orientation is of an excited dipole. What matters is only the total number of excited fluorophores in a region corresponding to a detector pixel regardless of their orientation. Another consequence of $Q_{\perp}/Q_{||}$ being close to 1 is that rotational diffusion of the fluorophore after excitation has little effect on the total amount of gathered light.

Theoretical details: specific geometry of exocytotic fusion model and optical resolution limitations

The goal is to calculate a theoretical *P* and *S* fluorescence from a realistic model of the fusion event as seen through a microscopic and recorded by a charge-coupled device (CCD) array rather than the idealized plane and sphere model. The exocytotic fusion structure we use to describe the stages of secretory granule fusion with the plasma membrane is modeled in this study as spherical surface of radius R truncated by a flat plane, as schematically shown near the bottom of Fig. 3 (the theoretical method to be described is also applicable to other geometries). This fusion structure is both complicated and on the same order of size as the microscope resolution

and the evanescent field depth, so the idealized model discussed in the text (submicroscopic pure sphere or pure plane) is not adequate for several reasons. Although the distribution of dil (1,1′-dioctadecyl-3,3,3′,3′-tetramethylindocarbocyanine perchlorate) may be azimuthally symmetric as integrated over the whole structure (as required in the previous section), it may not be so symmetric in resolvable subregions. The TIRF illumination intensity, which decreases exponentially with distance from the substrate, may vary significantly over the indentation produced by the fusion. The local azimuthal asymmetry, tangential foreshortening, and uneven illumination may be partially resolvable, but these features are significantly blurred by structure by optical resolution limitations. The dil dipole may not lie exactly in the plane of the membrane. Lastly, the actual image on a digital camera is noticeably pixelated over the size of a fusion site (several hundred nanometers).

To take these effects into account, we do not use the orientational distribution $\eta(\theta,\phi)$ approach as in the idealized model, but instead we consider the vectorial components (M_x, M_y, and M_z) of the dipole moment, M, of dil at each location on the fusion structure. The dil dipoles are assumed to be distributed with azimuthal symmetry at some fixed angle, β, relative to the normal to the membrane at each location (e.g., for dil dipoles exactly parallel to the local membrane plane, β would be 90°). Any location on the spherical part of the structure can be identified by its polar coordinates (θ,ϕ). The azimuthal angle of any particular dipole around the local membrane normal is denoted by ψ. Use of rotation matrices allows calculation of the vectorial components for both the spherical and planar parts of the fusion structure. For the spherical part,

$$M_x(sphere) = \cos\theta\cos\phi\sin\beta\cos\psi - \sin\theta\cos\phi\cos\beta - \sin\phi\sin\psi\sin\beta,$$
$$M_y(sphere) = \cos\theta\sin\phi\sin\beta\cos\psi - \sin\theta\sin\phi\cos\beta + \cos\phi\sin\psi\sin\beta,$$
$$M_z(sphere) = \sin\theta\sin\beta\cos\psi + \cos\theta\cos\beta.$$

For the planar part,

$$M_x(plane) = \sin\beta\cos\psi,$$
$$M_y(plane) = \sin\beta\sin\psi,$$
$$M_z(plane) = \cos\beta.$$

Because the fluorescence is to be viewed with a very high aperture objective through which the emissions from all excited fluorophores are collected with equal efficiency regardless of orientation, the only important issue is how many dipoles are excited by a particular excitation polarization at each point in the fusion structure. That number is proportional to the square of the component of the absorption dipole in the polarization direction of the excitation, averaged over the azimuthal angles ψ around the local membrane normal. The number of s-pol and p-pol excited fluorophores at any location is thereby proportional to $\langle M_y^2 \rangle$ and $\langle M_z^2 \rangle$, respectively, where the brackets denote averaging over ψ. The squaring step for the spherical part leads to numerous cross terms, which all become zero upon averaging over ψ, leaving only the square terms. Tangential viewing along the edge of the sphere must also be taken into account, whereby more membrane is in the view of a particular image pixel by a multiplicative factor of $(1/\cos\theta)$. Under these conditions, the raw emission intensities *S′* and *P′* (meaning before evanescent field depth and optical resolution are taken into account) for s-pol and p-pol, respectively, are (with all constants suppressed)

$$S'(sphere) = \frac{1}{2\cos\theta}\left(\cos^2\theta\sin^2\phi\sin^2\beta + 2\sin^2\theta\sin^2\phi\cos^2\beta + \cos^2\phi\sin^2\beta\right),$$
$$P'(sphere) = \frac{1}{2\cos\theta}\left(\sin^2\theta\sin^2\beta + 2\cos^2\theta\cos^2\beta\right),$$
$$S'(plane) = \frac{1}{2}\sin^2\beta,$$
$$P'(plane) = \cos^2\beta. \qquad (6)$$

Based on these formulas, we created computer simulations of p-pol and s-pol excited images using a program custom written in interactive data language (IDL). The depth of the spherical indentation is measured by the distance z_d from the planar membrane to the top of the sphere, varying from 0 (no indentation) to 2R (a complete sphere with the fusion pore almost closed). For $z_d > R$, the local contribution to the fluorescence intensity comes from three separate locations: the planar membrane tucked underneath the truncated sphere (assumed to be flat against the substrate), the lower hemisphere of the sphere, and the upper hemisphere. In general, the fluorescence contributions (given for each point on the fusion structure by Eq. 6) are weighted by the exponentially decaying evanescent intensity. The two simulated fluorescence images (one for p-pol and one for s-pol) generated over a square area with a side of 2R are convolved with an optical point-spread function (an Airy disk) with a width expected from the objective's NA of 1.49. The images are binned into theoretical pixels of a size (relative to the spherical radius) corresponding to the actual experimental pixel size as would be seen by a CCD camera in our actual optical system. Fig. 3 shows examples of these simulated point-spread function–convolved images along with a grid indicating the pixelation for z_d = 1.75R. The total integrated intensity of all the pixels within a defined radius in each simulated image (the same radius as actually used on experimental data) is denoted as *P* and *S*, respectively, and the combinations *P/S* and *P+2S* are plotted in Fig. 4 as a function of indentation depth z_d. For this simulation, the orientation of the dil dipole was estimated to be 69° from the normal to the bilayer to match experimental measurements in HEK cells in regions where the plasma membrane is presumed to be flat (see Results).

Chromaffin cell preparation and transfection

Chromaffin cell preparation from bovine adrenal medulla and transient transfection were performed as described previously (Wick et al., 1993; Holz et al., 1994). Cells were plated onto 25-mm coverslips (refractive index 1.51) that had been coated with poly-D-lysine and calf skin collagen to promote cell adhesion. Cells were transfected with plasmid encoding NPY-Cer by Ca^{2+} phosphate precipitation (Wilson et al., 1995). The super-ecliptic pHluorin was inserted into the lumenal-facing domain (between transmembrane domains 1 and 2) of the rat VMAT2 sequence (Liu et al., 1992). The parent NPY plasmid was provided by W. Almers (Vollum Institute, Oregon Health and Science University, Portland, OR). NPY-Cer is a soluble lumenal marker of chromaffin granules that is released upon exocytosis. Experiments were performed 3–7 d after transfection.

Perfusion

Experiments were performed in a physiological salt solution (PSS) containing 145 mM NaCl, 5.6 mM KCl, 2.2 mM $CaCl_2$, 0.5 mM $MgCl_2$, and 15 mM Hepes, pH 7.4, at ∼28°C. Solution was delivered to individual cells through a pipet (100-µm inner diameter) using positive pressure from a computer-controlled perfusion system DAD-6VM (ALA Scientific Instruments). Generally, cells were perfused with PSS for 10 s and stimulated to secrete with elevated K^+-containing solution (95 mM NaCl, 56 mM KCl, 5 mM $CaCl_2$, 0.5 mM $MgCl_2$, and 15 mM Hepes, pH 7.4). Where used, *dynasore* was added directly to PSS to a final concentration of 80 mM (Macia et al., 2006; Newton et al., 2006). Bafilomycin A1 (GE Healthcare) was added to PSS to a final concentration of 1 mM. DiI-C18 (Sigma-Aldrich) was dissolved in ethanol to make a 1 mM stock solution. DiI was added directly to cells bathed in PSS at a 1:50 dilution. The cells were quickly washed several times in PSS and used immediately.

dil-labeled beads

To label beads with dil, 200-nm diameter nanospheres (Duke Scientific) were incubated in ethanolic dil and washed in PSS.

TIRFM

Prism-less (through the objective) TIRFM was obtained by directing an Argon ion (514 nm) or solid-state (442 nm) laser (CVI Melles Griot) through a custom side port to a side-facing dichroic mirror z442/514rpc and z442/514m emission filter (Chroma Technology Corp.) on an inverted microscope (IX70; Olympus) with the 1.5× internal magnifying lens in the emission path. The beam was focused on the periphery of the back focal plane of a 60× 1.49 NA oil immersion objective (Olympus) so that the laser beam was incident on the coverslip at ∼70° from the normal, giving a decay constant for the evanescent field of ∼110 nm. The band widths of the emissions were 450–490 (Cer) and 530–600 nm (Cer and Dil). Digital images were captured on a cooled EM CCD camera (Andor iXon; Andor Technology).

Excitation polarization optics

Fig. S1 shows the optical setup used to create the p-pol and s-pol 514-nm beams, superimpose their paths, and further superimpose the 442-nm beam on that path. Each of the three beam types is mechanically shuttered independently. The system is programmed to step through a sequence of three openings (one at a time), repeating the cycle without additional delay. The camera takes an exposure synchronous with each shutter opening. Images were acquired at ∼6.4 Hz with 50-ms exposures and 100 gain (EM setting). At 6.4 Hz, the full cycle of three exposures had a period of 454 ms.

Image analysis

Sequential NPY-Cer, dil s-, and p-polarized emission images were captured using IQ software (Andor Technology). Normalized *P/S* ratios (see following paragraph) and *P+2S* sums were calculated pixel by pixel for each image, and the transformations were aligned to the NPY-Cer images using custom software written in IDL. Exocytosis of individual granules was evident from the sudden and complete loss of NPY-Cer fluorescence. Changes in *P/S* and *P+2S* were determined in a 292-nm radius ROI centered over localized increases in the *P/S* ratio at sites of exocytosis. When fusion occurred without an evident increase in *P/S*, the ROI was centered over the region of the fusing granule.

P/S varies with the relative intensities of the p- and s-pol excitations, biases in the optical system, and interference fringes. To reduce these effects and allow comparisons with theory, *P/S* ratios from the dil emission were normalized to the ratio obtained with solution containing 10 mM rhodamine 6G (Invitrogen), which is predicted to be randomly oriented. The normalization was performed using the mean of the p- and s-polarized rhodamine 6G emissions.

For the purposes of estimating noise in *P/S* and to set a threshold above which changes in *P/S* are significant, the *P/S* of nonfusing granules within three ROIs of fusing granules was determined at the time of fusion of the neighboring granule. Changes in the *P/S* for the nonfusing granules had a standard deviation of 2% (50 granules). Changes >6% had a high probability of being significant.

To calculate the distance between the cover glass and chromaffin cell footprint, fluorophore exclusion experiments were performed with Oregon green dextran (Invitrogen) in TIRF. Distances were found to vary between 40 and 80 nm.

Lateral distance between the last granule position and the subsequent *P/S* increase was determined on NPY-Cer and dil ratio images that were filtered to suppress high and low spatial frequency variation. An automated search identified the dil ratio maximum in the vicinity of the Cer maximum to single-pixel accuracy (pixel size = 73 nm). A center of intensity procedure (custom written in IDL) further extrapolated the center of both the NPY-Cer–labeled granule and the p/s ratio increase. Graphs were drawn with Prism 5 (GraphPad Software, Inc.).

Online supplemental material

Fig. S1 shows a schematic of the pTIRFM optical system. Fig. S2 shows static images of a chromaffin cell membrane stained with dil and exposed sequentially to 442 and 514 s- and p-polarized light. Fig. S3 provides three examples of different changes detected in membrane *P/S* and *P+2S* upon exocytosis. Fig. S4 shows the percentage increase in *P+2S* from before fusion to 1 s after fusion for control and dynasore-treated cells. Online supplemental material is available at http://www.jcb.org/cgi/content/full/jcb.200908010/DC1.

We wish to thank Dr. Tomas Kirchhausen (Harvard Medical School) for generously providing the *Dynasore* reagent. We are indebted to Dr. Mary A. Bittner and Rachel Aikman for carefully reading the manuscript.

This research used the Sequencing Core of the Michigan Diabetes Research and Training Center supported by DK20572. This work was supported by a National Institutes of Health (NIH) grant (R01-NS38129 to R.W. Holz and D. Axelrod) and fellowships (5T32DA007268 and 1F32GM086169 to A. Anantharam). This work was also supported by NIH grants from the National Institute of Mental Health (MH50712) and National Institute on Drug Abuse (DA10154) to R.H. Edwards.

Submitted: 3 August 2009
Accepted: 10 January 2010

References

Allersma, M.W., L. Wang, D. Axelrod, and R.W. Holz. 2004. Visualization of regulated exocytosis with a granule-membrane probe using total internal reflection microscopy. *Mol. Biol. Cell.* 15:4658–4668. doi:10.1091/mbc.E04-02-0149

Allersma, M.W., M.A. Bittner, D. Axelrod, and R.W. Holz. 2006. Motion matters: secretory granule motion adjacent to the plasma membrane and exocytosis. *Mol. Biol. Cell.* 17:2424–2438. doi:10.1091/mbc.E05-10-0938

Artalejo, C.R., A. Elhamdani, and H.C. Palfrey. 2002. Sustained stimulation shifts the mechanism of endocytosis from dynamin-1-dependent rapid endocytosis to clathrin- and dynamin-2-mediated slow endocytosis in chromaffin cells. *Proc. Natl. Acad. Sci. USA.* 99:6358–6363. doi:10.1073/pnas.082658499

Axelrod, D. 1979. Carbocyanine dye orientation in red cell membrane studied by microscopic fluorescence polarization. *Biophys. J.* 26:557–573. doi:10.1016/S0006-3495(79)85271-6

Axelrod, D. 2001. Total internal reflection fluorescence microscopy in cell biology. *Traffic.* 2:764–774. doi:10.1034/j.1600-0854.2001.21104.x

Burghardt, T.P., and N.L. Thompson. 1984. Effect of planar dielectric interfaces on fluorescence emission and detection. Evanescent excitation with high-aperture collection. *Biophys. J.* 46:729–737. doi:10.1016/S0006-3495(84)84071-0

Burke, N.V., W. Han, D. Li, K. Takimoto, S.C. Watkins, and E.S. Levitan. 1997. Neuronal peptide release is limited by secretory granule mobility. *Neuron.* 19:1095–1102. doi:10.1016/S0896-6273(00)80400-6

Coupland, R.E. 1968. Determining sizes and distribution of sizes of spherical bodies such as chromaffin granules in tissue sections. *Nature.* 217:384–388. doi:10.1038/217384a0

Degtyar, V.E., M.W. Allersma, D. Axelrod, and R.W. Holz. 2007. Increased motion and travel, rather than stable docking, characterize the last moments before secretory granule fusion. *Proc. Natl. Acad. Sci. USA.* 104:15929–15934. doi:10.1073/pnas.0705406104

Ferguson, S.M., G. Brasnjo, M. Hayashi, M. Wölfel, C. Collesi, S. Giovedi, A. Raimondi, L.W. Gong, P. Ariel, S. Paradise, et al. 2007. A selective activity-dependent requirement for dynamin 1 in synaptic vesicle endocytosis. *Science.* 316:570–574. doi:10.1126/science.1140621

Fernández-Alfonso, T., and T.A. Ryan. 2004. The kinetics of synaptic vesicle pool depletion at CNS synaptic terminals. *Neuron.* 41:943–953. doi:10.1016/S0896-6273(04)00113-8

Fulop, T., S. Radabaugh, and C. Smith. 2005. Activity-dependent differential transmitter release in mouse adrenal chromaffin cells. *J. Neurosci.* 25:7324–7332. doi:10.1523/JNEUROSCI.2042-05.2005

Fulop, T., B. Doreian, and C. Smith. 2008. Dynamin I plays dual roles in the activity-dependent shift in exocytic mode in mouse adrenal chromaffin cells. *Arch. Biochem. Biophys.* 477:146–154. doi:10.1016/j.abb.2008.04.039

Graham, M.E., D.W. O'Callaghan, H.T. McMahon, and R.D. Burgoyne. 2002. Dynamin-dependent and dynamin-independent processes contribute to the regulation of single vesicle release kinetics and quantal size. *Proc. Natl. Acad. Sci. USA.* 99:7124–7129. doi:10.1073/pnas.102645099

Han, W., Y.K. Ng, D. Axelrod, and E.S. Levitan. 1999. Neuropeptide release by efficient recruitment of diffusing cytoplasmic secretory vesicles. *Proc. Natl. Acad. Sci. USA.* 96:14577–14582. doi:10.1073/pnas.96.25.14577

Hellen, E.H., and D. Axelrod. 1987. Fluorescence emission at dielectric and metal-film interfaces. *J. Opt. Soc. Am. B.* 4:337–350. doi:10.1364/JOSAB.4.000337

Henkel, A.W., and W. Almers. 1996. Fast steps in exocytosis and endocytosis studied by capacitance measurements in endocrine cells. *Curr. Opin. Neurobiol.* 6:350–357. doi:10.1016/S0959-4388(96)80119-X

Holz, R.W., R.A. Senter, and R.R. Sharp. 1983. Evidence that the H^+ electrochemical gradient across membranes of chromaffin granules is not involved in exocytosis. *J. Biol. Chem.* 258:7506–7513.

Holz, R.W., W.H. Brondyk, R.A. Senter, L. Kuizon, and I.G. Macara. 1994. Evidence for the involvement of Rab3A in $Ca^{(2+)}$-dependent exocytosis from adrenal chromaffin cells. *J. Biol. Chem.* 269:10229–10234.

Jaiswal, J.K., V.M. Rivera, and S.M. Simon. 2009. Exocytosis of post-Golgi vesicles is regulated by components of the endocytic machinery. *Cell.* 137:1308–1319. doi:10.1016/j.cell.2009.04.064

Liu, Y.J., D. Peter, A. Roghani, S. Schuldiner, G.G. Privé, D. Eisenberg, N. Brecha, and R.H. Edwards. 1992. A cDNA that suppresses MPP+ toxicity encodes a vesicular amine transporter. *Cell.* 70:539–551. doi:10.1016/0092-8674(92)90425-C

Macia, E., M. Ehrlich, R. Massol, E. Boucrot, C. Brunner, and T. Kirchhausen. 2006. Dynasore, a cell-permeable inhibitor of dynamin. *Dev. Cell.* 10:839–850. doi:10.1016/j.devcel.2006.04.002

Mattheyses, A.L., and D. Axelrod. 2006. Direct measurement of the evanescent field profile produced by objective-based total internal reflection fluorescence. *J. Biomed. Opt.* 11:014006.

Newton, A.J., T. Kirchhausen, and V.N. Murthy. 2006. Inhibition of dynamin completely blocks compensatory synaptic vesicle endocytosis. *Proc. Natl. Acad. Sci. USA.* 103:17955–17960. doi:10.1073/pnas.0606212103

Ohara-Imaizumi, M., Y. Nakamichi, T. Tanaka, H. Ishida, and S. Nagamatsu. 2002. Imaging exocytosis of single insulin secretory granules with evanescent wave microscopy: distinct behavior of granule motion in biphasic insulin release. *J. Biol. Chem.* 277:3805–3808. doi:10.1074/jbc.C100712200

Oheim, M., D. Loerke, W. Stuhmer, and R.H. Chow. 1998. The last few milliseconds in the life of a secretory granule. Docking, dynamics and fusion visualized by total internal reflection fluorescence microscopy (TIRFM). *Eur. Biophys. J.* 27:83–98. doi:10.1007/s002490050114

Oreopoulos, J., and C.M. Yip. 2009. Combinatorial microscopy for the study of protein-membrane interactions in supported lipid bilayers: order parameter measurements by combined polarized TIRFM/AFM. *J. Struct. Biol.* 168:21–36. doi:10.1016/j.jsb.2009.02.011

Perrais, D., I.C. Kleppe, J.W. Taraska, and W. Almers. 2004. Recapture after exocytosis causes differential retention of protein in granules of bovine chromaffin cells. *J. Physiol.* 560:413–428. doi:10.1113/jphysiol.2004.064410

Schmoranzer, J., M. Goulian, D. Axelrod, and S.M. Simon. 2000. Imaging constitutive exocytosis with total internal reflection fluorescence microscopy. *J. Cell Biol.* 149:23–32. doi:10.1083/jcb.149.1.23

Shakiryanova, D., A. Tully, R.S. Hewes, D.L. Deitcher, and E.S. Levitan. 2005. Activity-dependent liberation of synaptic neuropeptide vesicles. *Nat. Neurosci.* 8:173–178. doi:10.1038/nn1377

Silverman, M.A., S. Johnson, D. Gurkins, M. Farmer, J.E. Lochner, P. Rosa, and B.A. Scalettar. 2005. Mechanisms of transport and exocytosis of dense-core granules containing tissue plasminogen activator in developing hippocampal neurons. *J. Neurosci.* 25:3095–3106. doi:10.1523/JNEUROSCI.4694-04.2005

Steyer, J.A., H. Horstmann, and W. Almers. 1997. Transport, docking and exocytosis of single secretory granules in live chromaffin cells. *Nature.* 388:474–478. doi:10.1038/41329

Sund, S.E., J.A. Swanson, and D. Axelrod. 1999. Cell membrane orientation visualized by polarized total internal reflection fluorescence. *Biophys. J.* 77:2266–2283. doi:10.1016/S0006-3495(99)77066-9

Sweitzer, S.M., and J.E. Hinshaw. 1998. Dynamin undergoes a GTP-dependent conformational change causing vesiculation. *Cell.* 93:1021–1029. doi:10.1016/S0092-8674(00)81207-6

Taraska, J.W., and W. Almers. 2004. Bilayers merge even when exocytosis is transient. *Proc. Natl. Acad. Sci. USA.* 101:8780–8785. doi:10.1073/pnas.0401316101

Taraska, J.W., D. Perrais, M. Ohara-Imaizumi, S. Nagamatsu, and W. Almers. 2003. Secretory granules are recaptured largely intact after stimulated exocytosis in cultured endocrine cells. *Proc. Natl. Acad. Sci. USA.* 100:2070–2075. doi:10.1073/pnas.0337526100

Terasaki, M. 1995. Visualization of exocytosis during sea urchin egg fertilization using confocal microscopy. *J. Cell Sci.* 108:2293–2300.

Thompson, N.L., H.M. McConnell, and T.P. Burhardt. 1984. Order in supported phospholipid monolayers detected by the dichroism of fluorescence excited with polarized evanescent illumination. *Biophys. J.* 46:739–747. doi:10.1016/S0006-3495(84)84072-2

Tsuboi, T., and G.A. Rutter. 2003. Multiple forms of "kiss-and-run" exocytosis revealed by evanescent wave microscopy. *Curr. Biol.* 13:563–567. doi:10.1016/S0960-9822(03)00176-3

Tsuboi, T., C. Zhao, S. Terakawa, and G.A. Rutter. 2000. Simultaneous evanescent wave imaging of insulin vesicle membrane and cargo during a single exocytotic event. *Curr. Biol.* 10:1307–1310. doi:10.1016/S0960-9822(00)00756-9

Tsuboi, T., H.T. McMahon, and G.A. Rutter. 2004. Mechanisms of dense core vesicle recapture following "kiss and run" ("cavicapture") exocytosis in insulin-secreting cells. *J. Biol. Chem.* 279:47115–47124. doi:10.1074/jbc.M408179200

Wick, P.F., R.A. Senter, L.A. Parsels, M.D. Uhler, and R.W. Holz. 1993. Transient transfection studies of secretion in bovine chromaffin cells and PC12 cells. Generation of kainate-sensitive chromaffin cells. *J. Biol. Chem.* 268:10983–10989.

Wick, P.F., J.M. Trenkle, and R.W. Holz. 1997. Punctate appearance of dopamine-β-hydroxylase on the chromaffin cell surface reflects the fusion of individual chromaffin granules upon exocytosis. *Neuroscience.* 80:847–860. doi:10.1016/S0306-4522(97)00062-6

Wilson, S.P., F. Liu, R.E. Wilson, and P.R. Housley. 1995. Optimization of calcium phosphate transfection for bovine chromaffin cells: relationship to calcium phosphate precipitate formation. *Anal. Biochem.* 226:212–220. doi:10.1006/abio.1995.1216

Winkler, H. 1977. The biogenesis of adrenal chromaffin granules. *Neuroscience.* 2:657–683.